Unconditionally stable finite-difference time-domain methods for modeling the Sagnac effect

Roman Novitski, Jacob Scheuer, and Ben Z. Steinberg
School of Electrical Engineering, Tel-Aviv University, Ramat Aviv, Tel-Aviv 69978, Israel
(Received 16 August 2012; revised manuscript received 15 November 2012; published 15 February 2013)

We present two unconditionally stable finite-difference time-domain (FDTD) methods for modeling the Sagnac effect in rotating optical microsensors. The methods are based on the implicit Crank-Nicolson scheme, adapted to hold in the rotating system reference frame—the rotating Crank-Nicolson (RCN) methods. The first method (RCN-2) is second order accurate in space whereas the second method (RCN-4) is fourth order accurate. Both methods are second order accurate in time. We show that the RCN-4 scheme is more accurate and has better dispersion isotropy. The numerical results show good correspondence with the expression for the classical Sagnac resonant frequency splitting when using group refractive indices of the resonant modes of a microresonator. Also we show that the numerical results are consistent with the perturbation theory for the rotating degenerate microcavities. We apply our method to simulate the effect of rotation on an entire Coupled Resonator Optical Waveguide (CROW) consisting of a set of coupled microresonators. Preliminary results validate the formation of a rotation-induced gap at the center of a transfer function of a CROW.

DOI: 10.1103/PhysRevE.87.023303 PACS number(s): 02.60.−x, 42.81.Pa, 42.55.Sa, 41.20.−q

I. INTRODUCTION

The effect of the additional phase accumulation by a light wave propagating in a mechanically rotating optical medium is known as the Sagnac effect [1]. Recently there has been an increased interest in the Sagnac effect manifested in rotating resonant microcavities and miniature photonic structures [2–4]. Usually the analysis of such structures involves either the use of the well known phenomenological expression of the Sagnac phase shift in a rotating circular optical medium [5,6], or derivations from the first principles using the Maxwell's equations in the rotating frame with further assumptions and simplifications in order to get closed form results [4,7,8]. There are a few numerical techniques which were proposed recently to analyze such problems. One such option is to use the two-dimensional (2D) Green's function theory for the electrodynamics of a rotating medium [8] in legacy codes of, e.g., the method of moments. Alternatively, two finite-difference time-domain algorithms based on the well known Yee's lattice and the leapfrog scheme were proposed. The first finite-difference time-domain (FDTD) method proposed by Peng *et al*. [9] incorporates time extrapolation in calculation of the electromagnetic fields. We believe that this approach makes the scheme unstable as illustrated in the Appendix for the case of the linear extrapolation. The FDTD method proposed by Sarma *et al*. [10] avoids this problem by incorporating D and B (in addition to the regular E and H fields) using time interpolation into their algorithm. But in order to keep the latter scheme stable there might be a need to simultaneously know both E and H in the entire rotating medium (they must satisfy the wave equation) when introducing sources to the simulation, which may prove to be not practical and may generate errors. Therefore we believe that these explicit FDTD methods are less suitable for application in rotating medium.

In this paper we present two unconditionally stable 2D FDTD algorithms for modeling Sagnac which are based on the Crank-Nicolson (CN) scheme [11]. In such a scheme the computational grid is based on Yee's lattice, but unlike the leapfrog scheme the values of all the fields are updated at the same time step. This approach avoids the need for any kind of extrapolation in time, since the Sagnac effect is modeled by using the values of the fields at the same time steps as for the regular CN scheme for the stationary case. As well, the scheme is based solely on calculation of E and H thus avoiding the need to incorporate D and B, and to estimate simultaneously both E and H in the entire rotating domain. Since the Sagnac effect is basically a phase modification effect, it might be susceptible to numerical dispersion errors inherently existing in any FDTD algorithm as a result of space and time discretizations. Therefore, we present two slightly different schemes in order to address this issue. The first method, called throughout this paper rotating Crank-Nicolson-2 (RCN-2), is second order accurate in space, while the second method, called RCN-4, has fourth order space accuracy. Both methods are second order accurate in time. The use of the fourth order accurate derivatives in space helps to decrease the numerical dispersion error, and as a result we get a more accurate modeling of the Sagnac effect. In order to demonstrate the effectiveness of the proposed methods and their differences, we apply them to a problem of a rotating microring resonator and compare the obtained results with the classical Sagnac expression for the frequency splitting and the results obtained in perturbation theories [4,7]. We also apply the RCN-4 scheme to a bigger problem of a rotating Coupled Resonator Optical Waveguide (CROW) of four resonators.

The structure of this paper is as follows. In Sec. II we present the formulation of the proposed methods. In Sec. III we analyze the stability and the numerical dispersion of the algorithms. We compare the performances of the two schemes, and as well we verify the obtained results against those predicted by the theory in Sec. IV. In this section we also simulate the effect of rotation on a CROW that consists of a set of coupled resonators. Concluding remarks are provided in Sec. V.

II. FORMULATIONS

We assume a two-dimensional slowly rotating medium at the x-y plane with a rotation rate Ω, so that the angular

velocity is

$$\vec{\Omega} = \hat{z}\Omega. \tag{2.1}$$

The assumption of slow rotation velocity implies that neither relativistic effects nor geometrical transformations take place and $|\vec{\Omega} \times \vec{r}| \ll c$, for the largest r in the simulated rotating medium, and c is the speed of light in vacuum. Therefore, operators such as $\vec{\nabla}$ are conserved in the rotating rest frame of reference: $\vec{\nabla} = \vec{\nabla}'$, and time is invariant in both systems: $t = t'$. According to a formal structure of electrodynamics, the basic physical laws governing the electromagnetic fields are invariant under any coordinate transformations, including a noninertial one [12,13]. The transformation to a rotating system is manifested only by an appropriate change of the constitutive relations. Therefore Maxwell's curl equations in the rotating frame R are given by

$$\vec{\nabla} \times \vec{E} = -\frac{\partial \vec{B}}{\partial t} - \sigma_m \vec{H}, \tag{2.2a}$$

$$\vec{\nabla} \times \vec{H} = \frac{\partial \vec{D}}{\partial t} - \sigma \vec{E}. \tag{2.2b}$$

Assuming the material properties at rest are given by ε, μ, then up to the first order in velocity the constitutive relations in R take on the form [12]

$$\vec{D} = \varepsilon \vec{E} - c^{-2}\vec{\Omega} \times \vec{r} \times \vec{H}, \tag{2.3a}$$

$$\vec{B} = \mu \vec{H} + c^{-2}\vec{\Omega} \times \vec{r} \times \vec{E}, \tag{2.3b}$$

where $\vec{r} = \hat{x}x + \hat{y}y$. After substituting Eq. (2.3) into the Eq. (2.2) and assuming a constant rotation rate ($\frac{\partial \vec{\Omega}}{\partial t} = 0$) and a fixed rotation axis ($\frac{\partial \vec{r}}{\partial t} = 0$), we get the following set of equations for the 2D case (where $\frac{\partial H}{\partial z} = \frac{\partial E}{\partial z} = 0$):

$$\mu \frac{\partial H_x}{\partial t} = -\frac{\partial E_z}{\partial y} - \sigma_m H_x - c^{-2}\Omega x \frac{\partial E_z}{\partial t}, \tag{2.4a}$$

$$\mu \frac{\partial H_y}{\partial t} = \frac{\partial E_z}{\partial x} - \sigma_m H_y - c^{-2}\Omega y \frac{\partial E_z}{\partial t}, \tag{2.4b}$$

$$\mu \frac{\partial H_z}{\partial t} = \frac{\partial E_x}{\partial y} - \frac{\partial E_y}{\partial x} - \sigma_m H_z + c^{-2}\Omega x \frac{\partial E_x}{\partial t} + c^{-2}\Omega y \frac{\partial E_y}{\partial t}, \tag{2.4c}$$

$$\varepsilon \frac{\partial E_x}{\partial t} = \frac{\partial H_z}{\partial y} - \sigma E_x + c^{-2}\Omega x \frac{\partial H_z}{\partial t}, \tag{2.4d}$$

$$\varepsilon \frac{\partial E_y}{\partial t} = -\frac{\partial H_z}{\partial x} - \sigma E_y + c^{-2}\Omega y \frac{\partial H_z}{\partial t}, \tag{2.4e}$$

$$\varepsilon \frac{\partial E_z}{\partial t} = \frac{\partial H_y}{\partial x} - \frac{\partial H_x}{\partial y} - \sigma E_z - c^{-2}\Omega y \frac{\partial H_y}{\partial t} - c^{-2}\Omega x \frac{\partial H_x}{\partial t}. \tag{2.4f}$$

It has been rigorously shown that in the 2D case these equations can be split into two independent transverse electric (TE) and transverse magnetic (TM) modes [8]. In this paper we concentrate on the TM mode (H_x,H_y,E_z) sustained by Eqs. (2.4a), (2.4b), and (2.4f). The case for the TE mode (E_x,E_y,H_z) can be obtained from the TM case by simple exchange of variables. Using Yee's meshing in the 2D case, which is shown in Fig. 1, both the RCN-2 and the RCN-4

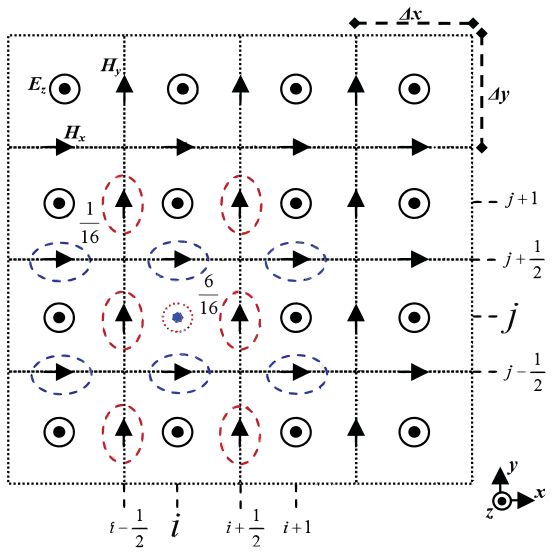

FIG. 1. (Color online) Yee's space lattice with the indicated magnetic field components (H_x,H_y) and their relative weights (for six-point interpolation) used to account for the Sagnac effect in the calculation of the electric field at the marked grid point (i,j) (dashed).

schemes for the TM wave can be written as

$$H_x^{n+1} = H_x^n - a_{1Hx} D_y\left(E_z^{n+1} + E_z^n\right) - a_{2Hx}\left(H_x^{n+1} + H_x^n\right) - a_{3Hx} S_y\left(E_z^{n+1} - E_z^n\right), \tag{2.5a}$$

$$H_y^{n+1} = H_y^n + a_{1Hy} D_x\left(E_z^{n+1} + E_z^n\right) - a_{2Hy}\left(H_y^{n+1} + H_y^n\right) - a_{3Hy} S_x\left(E_z^{n+1} - E_z^n\right), \tag{2.5b}$$

$$E_z^{n+1} = E_z^n + a_{1Ezx} D_x\left(H_y^{n+1} + H_y^n\right) - a_{1Ezy} D_y\left(H_x^{n+1} + H_x^n\right) - a_{2Ez}\left(E_z^{n+1} + E_z^n\right) - a_{3Ezx} S_x\left(H_y^{n+1} - H_y^n\right) - a_{3Ezy} S_y\left(H_x^{n+1} - H_x^n\right), \tag{2.5c}$$

where the coefficients $a_\#$ are given as

$$a_{1Hx} = \frac{\Delta t}{2\Delta y \mu}, \quad a_{2Hx} = \frac{\Delta t \sigma_m}{2\mu}, \quad a_{3Hx} = \frac{c^{-2}\Omega x}{\mu}, \tag{2.6a}$$

$$a_{1Hy} = \frac{\Delta t}{2\Delta x \mu}, \quad a_{2Hy} = \frac{\Delta t \sigma_m}{2\mu}, \quad a_{3Hy} = \frac{c^{-2}\Omega y}{\mu}, \tag{2.6b}$$

$$a_{1Ezx} = \frac{\Delta t}{2\Delta x \varepsilon}, \quad a_{1Ezy} = \frac{\Delta t}{2\Delta y \varepsilon}, \quad a_{2Ez} = \frac{\Delta t \sigma}{2\varepsilon}, \quad a_{3Ezx} = \frac{c^{-2}\Omega y}{\varepsilon}, \quad a_{3Ezy} = \frac{c^{-2}\Omega x}{\varepsilon}, \tag{2.6c}$$

and the operators D_x, D_y are the difference operators along the x axis and the y axis, respectively, while the operators S_x, S_y are the sum operators along those axes needed to account for rotation (together with the coefficients a_3). The need for the latter operators results from the fact that we must know the values of the fields in the points which are not given in the computational grid. For example, in order to calculate E_z we need the values of H_x and H_y at the same point. A simple way to calculate the fields in those "in-between" points is to use the

linear interpolation by taking the average of the values in the existing grid points, which is to use two points with a relative weight of 1/2. But we can obtain a better approximation if we use more points for the interpolation. The simulations carried out in this paper use six-point interpolation for this purpose. For example, when calculating the value of $E^{n+1}_{z(i,j)}$ in Eq. (2.5c), the terms $S_x H_y^{n+1}$ and $S_y H_x^{n+1}$ will give the values of $H^{n+1}_{y(i,j)}$ and $H^{n+1}_{x(i,j)}$ at the point (i,j) as

$$S_x H_y^{n+1}\big|_{(i,j)} = H^{n+1}_{y(i,j)} = \frac{H^{n+1}_{y(i+1/2,j+1)} + 6H^{n+1}_{y(i+1/2,j)} + H^{n+1}_{y(i+1/2,j-1)} + H^{n+1}_{y(i-1/2,j+1)} + 6H^{n+1}_{y(i-1/2,j)} + H^{n+1}_{y(i-1/2,j-1)}}{16}, \tag{2.7a}$$

$$S_y H_x^{n+1}\big|_{(i,j)} = H^{n+1}_{x(i,j)} = \frac{H^{n+1}_{x(i-1,j+1/2)} + 6H^{n+1}_{x(i,j+1/2)} + H^{n+1}_{x(i+1,j+1/2)} + H^{n+1}_{x(i-1,j-1/2)} + 6H^{n+1}_{x(i,j-1/2)} + H^{n+1}_{x(i+1,j-1/2)}}{16}. \tag{2.7b}$$

The latter equation is illustrated in Fig. 1, where the calculation of $E^{n+1}_{z(i,j)}$ uses the closest samples of the magnetic fields with the relative weights of 6/16 and the further ones with the weights of 1/16. A similar procedure is used for the calculation of the magnetic fields by Eqs. (2.5a) and (2.5b).

We should point out that both the coefficients $a_\#$ and the operators in Eqs. (2.5) are represented by sparse matrices and the electromagnetic fields are column vectors. The choice between the second order and the forth order accuracies in space is done by the use of the appropriate implementation of the differentiating operators D_x, D_y using central differences. By rearranging Eqs. (2.5a) and (2.5b) and substituting them into Eq. (2.5c), we arrive at the following set of equations:

$$H_x^{n+1} = \frac{(1-a_{2Hx})}{(1+a_{2Hx})} H_x^n - \frac{(a_{1Hx}D_y - a_{3Hx}S_y)}{(1+a_{2Hx})} E_z^n - \frac{(a_{1Hx}D_y + a_{3Hx}S_y)}{(1+a_{2Hx})} E_z^{n+1}, \tag{2.8a}$$

$$H_y^{n+1} = \frac{(1-a_{2Hy})}{(1+a_{2Hy})} H_y^n + \frac{(a_{1Hy}D_x + a_{3Hy}S_x)}{(1+a_{2Hy})} E_z^n + \frac{(a_{1Hy}D_x - a_{3Hy}S_x)}{(1+a_{2Hy})} E_z^{n+1}, \tag{2.8b}$$

$$\begin{aligned}
&\left[I - \frac{(a_{1Ezx}D_x - a_{3Ezx}S_x)}{(1+a_{2Ez})}\frac{(a_{1Hy}D_x - a_{3Hy}S_x)}{(1+a_{2Hy})} - \frac{(a_{1Ezy}D_y + a_{3Ezy}S_y)}{(1+a_{2Ez})}\frac{(a_{1Hx}D_y + a_{3Hx}S_y)}{(1+a_{2Hx})}\right] E_z^{n+1} \\
&\quad = \left[\frac{(1-a_{2Ez})}{(1+a_{2Ez})} + \frac{(a_{1Ezx}D_x - a_{3Ezx}S_x)}{(1+a_{2Ez})}\frac{(a_{1Hy}D_x + a_{3Hy}S_x)}{(1+a_{2Hy})} + \frac{(a_{1Ezy}D_y + a_{3Ezy}S_y)}{(1+a_{2Ez})}\frac{(a_{1Hx}D_y - a_{3Hx}S_y)}{(1+a_{2Hx})}\right] E_z^n \\
&\qquad + \left[(a_{1Ezx}D_x + a_{3Ezx}S_x) + \frac{(a_{1Ezx}D_x - a_{3Ezx}S_x)}{(1+a_{2Ez})}\frac{(1-a_{2Hy})}{(1+a_{2Hy})}\right] H_y^n \\
&\qquad - \left[(a_{1Ezy}D_y + a_{3Ezy}S_y) + \frac{(a_{1Ezy}D_y + a_{3Ezy}S_y)}{(1+a_{2Ez})}\frac{(1-a_{2Hx})}{(1+a_{2Hx})}\right] H_x^n.
\end{aligned} \tag{2.8c}$$

Note that Eq. (2.8c) contains only the value of the electric field at the next time step $n+1$. Therefore, after solving it and putting the value of E_z^{n+1} into Eqs. (2.8a) and (2.8b) we get the magnetic fields H_x^{n+1} and H_y^{n+1}. Thus, the major computational obstacle is the solution of Eq. (2.8c) which was previously treated in the literature as the regular (stationary, nonrotating case) Crank-Nicolson scheme with the application of the Douglas-Gunn algorithm [14], which results in factorization of the left-hand side of the equation. Unfortunately, we cannot perform similar factorization here because of the additional terms accounting for the rotation. Therefore, we need another approach. Rewriting Eq. (2.8c) in a short form as

$$(I - M')E_z^{n+1} = ME_z^{n+1} = V^n, \tag{2.9}$$

where V^n is the resulting vector of the right-hand side of the equation that depends solely on the fields at the previous time step, and $M = I - M'$ is the matrix on the left-hand side. Note that this matrix is sparse. Since solving Eq. (2.9) at each time step is computationally expensive, we use the Neumann series expansion to approximately calculate the inverse as

$$M^{-1} = (I - M')^{-1} = \sum_{n=0}^{\infty} M'^n. \tag{2.10}$$

This expansion converges if $\|M'\| < 1$ in some consistent norm [15]. Once the inverse is calculated, it can be used for marching in time in Eqs. (2.8a)–(2.8c) without the need to fully solve Eq. (2.9) at each time step. One disadvantage of such approach is that the condition $\|M'\| < 1$ limits the value of the time step for which Eq. (2.10) can be used, since the norm grows with Δt. If a greater time step is required then Eq. (2.9) may be solved by the conventional iterative or direct methods, such as successive over-relaxation (SOR) or Gaussian elimination. However, using greater time steps increases the numerical dispersion error, and since the purpose of the proposed method is to account for the Sagnac phase shift in rotating systems, one should not use a very high value of Δt as the Sagnac effect may be screened by the numerical phase errors. The later is of special importance for low rotation rates.

Another disadvantage of using Eq. (2.10) is that the summation must be truncated in any practical implementation.

The use of the approximately computed propagation matrix may compromise the stability of the schemes as well as increase their numerical dispersion errors. In the simulations carried out in this paper we used the first five terms of the series, which resulted in the maximum error of 0.01% in the calculated values of the fields in the computational grid, without any observable instability within the run times. We believe that the number of terms used in the series must be increased when one uses greater computational grids than those in this paper in order to preserve the same accuracy and stability. We emphasize that the excitation of the presented scheme is straightforward since both E and H are evaluated at the same time step. For instance, assuming certain spatial and temporal distributions of E_z^{n+1} along a specific plane at the grid (for example, a waveguide's cross-section electric field profile, with a modulated Gaussian pulse temporal dependence), the corresponding values of H_x^{n+1} and H_y^{n+1} can be calculated from Eqs. (2.8a) and (2.8b), which will immediately satisfy the wave equation in the rotating medium.

III. STABILITY AND NUMERICAL DISPERSION

Both stability and numerical dispersion of the algorithms can be analyzed using the Fourier transform method [14]. We can rewrite Eq. (2.5) in the matrix form for the free space case as

$$\begin{bmatrix} 1 & 0 & (a_{1Hx}D_y + a_{3Hx}S_y) \\ 0 & 1 & -(a_{1Hy}D_x - a_{3Hy}Sx) \\ (a_{1Ezy}D_y + a_{3Ezy}S_y) & -(a_{1Ezx}D_x - a_{3Ezx}S_x) & 1 \end{bmatrix} \begin{pmatrix} H_x^{n+1} \\ H_y^{n+1} \\ E_z^{n+1} \end{pmatrix} = \begin{bmatrix} 1 & 0 & -(a_{1Hx}D_y - a_{3Hx}S_y) \\ 0 & 1 & (a_{1Hy}D_x + a_{3Hy}Sx) \\ -(a_{1Ezy}D_y - a_{3Ezy}S_y) & (a_{1Ezx}D_x + a_{3Ezx}S_x) & 1 \end{bmatrix} \begin{pmatrix} H_x^{n} \\ H_y^{n} \\ E_z^{n} \end{pmatrix}. \tag{3.1}$$

The last equation is general and holds for both RCN-2 and RCN-4 schemes. After applying the Fourier transform to the last equation, and further considering the RCN-2 scheme with the interpolation as shown in Eq. (2.7) we get

$$\begin{pmatrix} 1 & 0 & A_{13} \\ 0 & 1 & A_{23} \\ A_{31} & A_{32} & 1 \end{pmatrix} \begin{pmatrix} \tilde{H}_x^{n+1} \\ \tilde{H}_y^{n+1} \\ \tilde{E}_z^{n+1} \end{pmatrix} = \begin{pmatrix} 1 & 0 & A_{13}^* \\ 0 & 1 & A_{23}^* \\ A_{31}^* & A_{32}^* & 1 \end{pmatrix} \begin{pmatrix} \tilde{H}_x^{n} \\ \tilde{H}_y^{n} \\ \tilde{E}_z^{n} \end{pmatrix}, \tag{3.2}$$

where the asterisk denotes the complex conjugate and

$$A_{13} = -\frac{j\Delta t}{\Delta y \mu_0} \sin\left(\frac{\beta_y \Delta y}{2}\right) + \frac{c^{-2}\Omega\,(m\Delta x)}{\mu_0} \cos\left(\frac{\beta_y \Delta y}{2}\right)\left[\frac{3}{4} + \frac{1}{4}\cos\left(\beta_x \Delta x\right)\right], \tag{3.3a}$$

$$A_{23} = \frac{j\Delta t}{\Delta x \mu_0} \sin\left(\frac{\beta_x \Delta x}{2}\right) + \frac{c^{-2}\Omega\,(n\Delta y)}{\mu_0} \cos\left(\frac{\beta_x \Delta x}{2}\right)\left[\frac{3}{4} + \frac{1}{4}\cos(\beta_y \Delta y)\right], \tag{3.3b}$$

$$A_{31} = -\frac{j\Delta t}{\Delta y \varepsilon_0} \sin\left(\frac{\beta_y \Delta y}{2}\right) + \frac{c^{-2}\Omega\,(m\Delta x)}{\varepsilon_0} \cos\left(\frac{\beta_y \Delta y}{2}\right)\left[\frac{3}{4} + \frac{1}{4}\cos\left(\beta_x \Delta x\right)\right], \tag{3.3c}$$

$$A_{32} = \frac{j\Delta t}{\Delta x \varepsilon_0} \sin\left(\frac{\beta_x \Delta x}{2}\right) + \frac{c^{-2}\Omega\,(n\Delta y)}{\varepsilon_0} \cos\left(\frac{\beta_x \Delta x}{2}\right)\left[\frac{3}{4} + \frac{1}{4}\cos(\beta_y \Delta y)\right], \tag{3.3d}$$

where (m,n) is the coordinate of any point in the x-y plane. So the fields' evolution in time is given by the matrix

$$P = \begin{pmatrix} 1 & 0 & A_{13} \\ 0 & 1 & A_{23} \\ A_{31} & A_{32} & 1 \end{pmatrix}^{-1} \begin{pmatrix} 1 & 0 & A_{13}^* \\ 0 & 1 & A_{23}^* \\ A_{31}^* & A_{32}^* & 1 \end{pmatrix}. \tag{3.4}$$

The amplification factor of the scheme is given by the spectral radius of the matrix P. Numerical calculations show that $|\lambda_{1,2,3}| = 1$ (up to an accuracy of 10^{-15}) for any combination of Δx, Δy, Δt, Ω, and (m,n), as long as the condition $\Omega R < c$ is satisfied, where $R = \sqrt{(m\Delta x)^2 + (n\Delta y)^2}$. The same result holds for the RCN-4 scheme. Therefore, both schemes are unconditionally stable and strictly nondissipative.

The dispersion relation of the RCN-2 scheme is given by

$$\frac{\tan^2(\omega\Delta t/2)}{(c\Delta t)^2}u = \frac{\sin^2(\beta_x \Delta x/2)}{\Delta x^2} + \frac{\sin^2(\beta_y \Delta y/2)}{\Delta y^2} + \left(\frac{\Omega y}{c}\right)\frac{\sin(\beta_x \Delta x)}{c\Delta x}\frac{\tan\left(\omega\Delta t/2\right)}{\Delta t}\left[\frac{3}{4} + \frac{1}{4}\cos(\beta_y \Delta y)\right] - \left(\frac{\Omega x}{c}\right)\frac{\sin(\beta_y \Delta y)}{c\Delta y}\frac{\tan(\omega\Delta t/2)}{\Delta t}\left[\frac{3}{4} + \frac{1}{4}\cos\left(\beta_x \Delta x\right)\right], \tag{3.5a}$$

and the dispersion relation of the RCN-4 scheme is given by

$$\frac{\tan^2(\omega\Delta t/2)}{(c\Delta t)^2}u = \frac{\left[\frac{9}{8}\sin(\beta_x\Delta x/2) - \frac{1}{24}\sin(3\beta_x\Delta x/2)\right]^2}{\Delta x^2} + \frac{\left[\frac{9}{8}\sin(\beta_y\Delta y/2) - \frac{1}{24}\sin(3\beta_y\Delta y/2)\right]^2}{\Delta y^2}$$
$$+ \left(\frac{\Omega y}{c}\right)\frac{\left[\frac{13}{12}\sin(\beta_x\Delta x) - \frac{1}{24}\sin(2\beta_x\Delta x)\right]}{c\Delta x}\frac{\tan(\omega\Delta t/2)}{\Delta t}\left[\frac{3}{4} + \frac{1}{4}\cos(\beta_y\Delta y)\right]$$
$$- \left(\frac{\Omega x}{c}\right)\frac{\left[\frac{13}{12}\sin(\beta_y\Delta y) - \frac{1}{24}\sin(2\beta_y\Delta y)\right]}{c\Delta y}\frac{\tan(\omega\Delta t/2)}{\Delta t}\left[\frac{3}{4} + \frac{1}{4}\cos(\beta_x\Delta x)\right], \tag{3.5b}$$

where u in Eqs. (3.5a) and (3.5b) is given by

$$u = 1 - \left(\frac{\Omega y}{c}\right)^2\cos^2\left(\frac{\beta_x\Delta x}{2}\right)\left[\frac{3}{4} + \frac{1}{4}\cos(\beta_y\Delta y)\right]^2 - \left(\frac{\Omega x}{c}\right)^2\cos^2\left(\frac{\beta_y\Delta y}{2}\right)\left[\frac{3}{4} + \frac{1}{4}\cos(\beta_x\Delta x)\right]^2,$$

and $|\beta| = \sqrt{\beta_x^2 + \beta_y^2}$ is the numerical propagation phase constant. As seen from the Eqs. (3.5a) and (3.5b), the dispersion relations depend on the rotation rate Ω and on the coordinates of the point in the computational grid. As we take the limit of $\Delta x, \Delta y, \Delta t \to 0$, Eqs. (3.5a) and (3.5b) converge to the dispersion relation for the rotating free space as

$$\left(\frac{\omega}{c}\right)^2\left[1 - \frac{\Omega^2(x^2+y^2)}{c^2}\right] = \beta_x^2\left[1 + \frac{2}{\beta_x}\left(\frac{\Omega y}{c}\right)\frac{\omega}{c}\right] + \beta_y^2\left[1 - \frac{2}{\beta_y}\left(\frac{\Omega x}{c}\right)\frac{\omega}{c}\right] = |\beta|^2 - 2\frac{\omega}{c}\left[\vec{\beta}\cdot\frac{(\vec{\Omega}\times\vec{r})}{c}\right]. \tag{3.6}$$

To clarify the dispersion features and their dependence on location, we express $\vec{r}$ as a sum of parallel and perpendicular (with respect to $\vec{\beta}$) components: $\vec{r} = \vec{r}_\parallel + \vec{r}_\perp$ where $\vec{\beta} \parallel \vec{r}_\parallel$ and $\vec{\beta}\perp\vec{r}_\perp$. Then Eq. (3.6) reduces to (we keep only terms that are first order in Ω)

$$\left(\frac{\omega}{c}\right)^2 = |\beta|^2 - 2\frac{\omega}{c^2}\vec{\beta}\cdot(\vec{\Omega}\times\vec{r}_\perp) \xrightarrow{|\vec{\Omega}\times\vec{r}|\ll c} \frac{\omega}{\beta c} = 1 - \hat{\beta}\cdot(\vec{\Omega}\times\vec{r}_\perp)\frac{1}{c}. \tag{3.7}$$

Here $\vec{\beta} = \beta\hat{\beta}$. The Sagnac effect in Eqs. (3.5)–(3.7) is expressed via the first order terms in $\frac{\Omega x}{c}$ and $\frac{\Omega y}{c}$. There is a good correspondence between the rotation-induced modification of the propagation constant β and the modified phase of the Green's function for the rotating medium [8] (where the second order terms were neglected). First, we take a closer look at the dispersion for the stationary case ($\Omega = 0$). Figure 2 shows the phase velocity normalized to the vacuum speed of light as a function of the angle of propagation in the grid for the schemes RCN-2, RCN-4 without rotation (designated CN-2 and CN-4, respectively) and the regular Yee's algorithm with the second order accuracies both in time and space. The plots are shown for three cases: $S = 1/8, 1/4, 1/2$ where $S = c\frac{\Delta t}{\Delta x}$ and $\Delta x = 0.06$ μm. The dispersion of the Crank-Nicolson based schemes is of an opposite direction than that of the regular FDTD. In those schemes the dispersion increases with Δt, whereas it decreases in Yee's FDTD. Also, the RCN-2 scheme has similar anisotropy in dispersion as Yee's algorithm. In terms of anisotropy, the RCN-4 scheme has the best behavior of the three, as its curves are almost flat. Therefore in applications where the light travels in a circular path, such as in ring resonators, using the RCN-4 scheme makes it easier to estimate the numerical dispersion error, which may prove critical when modeling the Sagnac effect at relatively low rotation rates. The decrease in phase velocity means that the waves travel more slowly in the grid and the accumulated Sagnac phase shift and hence their resonance frequency splitting (when traveling in the opposite directions) will be lower. A similar plot as in Fig. 2 can be obtained for the numerical group velocity. The group velocity has the same behavior as the phase velocity; therefore we do not show it here. In order to demonstrate the x-y dependence of the dispersion relation on the rotation, in Fig. 3 we plot the phase velocity in the rotating medium normalized to c, found from Eq. (3.7). Note that the dispersion depends only on the *normal* distance from the rotation axis (normal with respect to the wave number).

We see that at the plane $x = y$ the phase velocity equals c, but as we go further from this plane, the velocity increases for

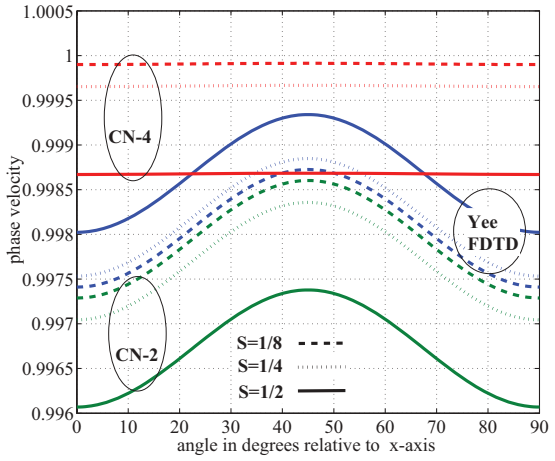

FIG. 2. (Color online) Phase velocity normalized to c for growing S values when $\Omega = 0$, $\Delta x = 0.06$ μm, $\lambda = 1.5$ μm vs the angle of propagation in the grid: CN-4 (red), CN-2 (green), and Yee's FDTD (blue).

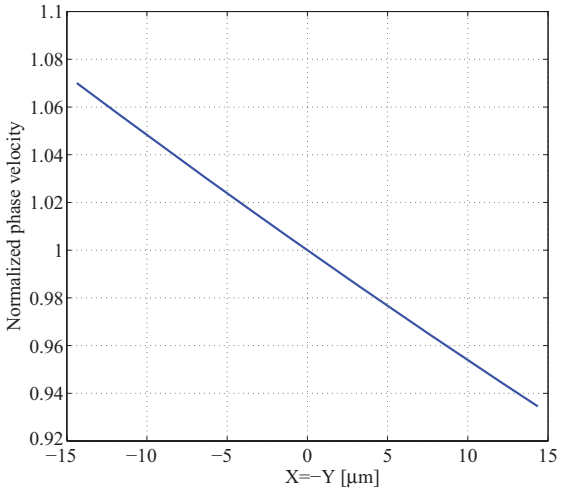

FIG. 3. (Color online) Phase velocity normalized to c for a wave traveling along the direction of $\theta = 45^\circ$ in the grid, for $\lambda = 1.5\ \mu$m and $\Omega = 10^{12}$ rad/s along the plane $y = -x$.

$x<y$ and it decreases for $x>y$. Figure 4 shows the errors (in percent) in phase velocities of the RCN-4 and RCN-2 schemes, relative to the exact phase velocity of the rotating medium for a wave traveling along the direction of $\theta = 45^\circ$, with $S = 1/2$, $\Delta x = 0.06\ \mu$m, $\lambda = 1.5\ \mu$m, and $\Omega = 10^{12}$ rad/s. The error is almost twice as large for the RCN-2 scheme.

Unfortunately, as was stated earlier, the Sagnac effect is sensitive to numerical dispersion errors; therefore techniques to eliminate those errors are required. One such technique would be to select such Δx, Δy, and Δt that those errors are zero for a specific set of frequencies or directions of propagation in the grid as shown in Ref. [16] for the regular explicit FDTD schemes. However, the structure of Eqs. (3.5a) and (3.5b) is such that similar dispersion reduction schemes cannot be applied, since the equations cannot be satisfied with any choice of a time step in order to get at least one frequency for which the dispersion is zero. We believe this is the result of the implicit nature of the schemes and hence the only way

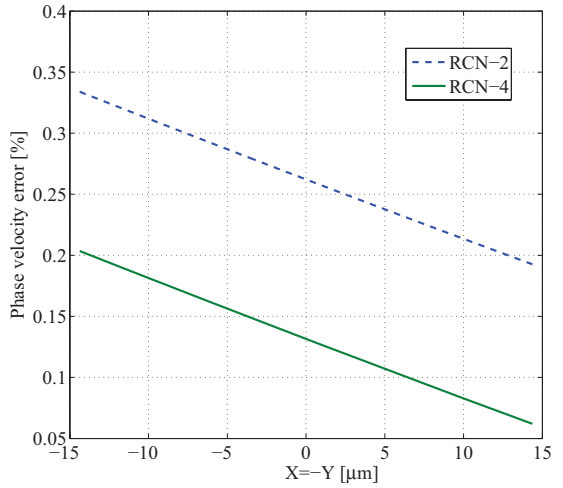

FIG. 4. (Color online) Phase velocity error (%) for RCN-2 and RCN4 for a wave traveling along the direction of $\theta = 45^\circ$ in the grid, for $\lambda = 1.5\ \mu$m and $\Omega = 10^{12}$ rad/s along the plane $y = -x$.

to reduce dispersion in the proposed two schemes is to use smaller time steps at the expense of a longer run time.

IV. NUMERICAL RESULTS

A. Single ring resonator

In this section we verify the ability of the proposed schemes to model the Sagnac effect and check the obtained results for consistency using the perturbation theory for rotating degenerate cavities derived in the previous work [7]. The simulations carried out in this section were performed in the structure of a ring resonator made of material with the refractive index $n = 3$ and having a radius of $R = 2\ \mu$m and width of $w = 0.4\ \mu$m. The computational grid consists of 320×320 points with $\Delta x = \Delta y = 0.02\ \mu$m, thus making it $6.4\ \mu\text{m} \times 6.4\ \mu$m in size. The excitation is done by inserting a profile of a modulated Gaussian pulse having center frequency and duration such that we get a number of excited resonant modes inside the resonator. The pulse is placed at "3 o'clock" in the resonator along the x axis. The electric field E_z is sampled at each time step at the opposite point inside the ring. The time step used is $\Delta t = 5/3 \times 10^{-5}$ ps, so that $S = 1/4$. Total time of the simulation is 140 ps, thus making it approximately 8.4×10^6 time steps. In order to minimize run time, our algorithm was implemented on a Tesla C2075 GPU (Nvidia) with JACKET software. Typical run time was about 9 h for a single resonator with the RCN-4 algorithm. Clearly, since we deal with an implicit procedure, running time is longer than that of an equivalent explicit approach. Unfortunately, run time data for other approaches *that apply to rotating systems* is not currently available in the literature.

Taking the Fourier transform of the sampled values of the field we get the spectrum from which the individual resonances of the resonator can be extracted. We also used Berenger's split-field formulation of the perfectly matched layer to implement the absorbing boundary conditions (ABC) [17]. Because of the rotation these ABCs suffer from reflections which are of order $\Omega R/c$, yet they give good results [9]. Further research is required to develop the ABCs in the rotating frame.

First, we check the linear dependence of the Sagnac frequency splitting on the rotation rate. The classical expression for the splitting is given by [18]

$$\delta\omega(\Omega) = \omega_0 \frac{\Omega R}{cn}, \tag{4.1}$$

where ω_0 is the stationary resonant frequency, R is the ring's radius, n is the refractive index of the medium, and c is the vacuum speed of light. In order to confirm the linear dependence of the splitting on the rotation rate, a number of simulations were performed using the RCN-4 scheme for the resonant mode $M = 23$. The first simulation was done for the zero rotation rate, that is, the stationary case, and four simulations with rotation rates which are multiples of $\Omega_0 = 5 \times 10^{10}$ rad/s. Figure 5 shows the distribution of the electric field at the end of the simulation (where $\Omega = 4 \times \Omega_0$) together with the edges of the resonator. Figure 6 shows the spectrum as a function of frequency. The resonant frequency of a stationary resonator can be found (the peak in the middle) as $f_0 = 201.5447$ THz with the effective index $n_{\text{eff}} = 2.7225$. The splitting at Ω_0 equals 42.9 GHz as shown in the figure. As

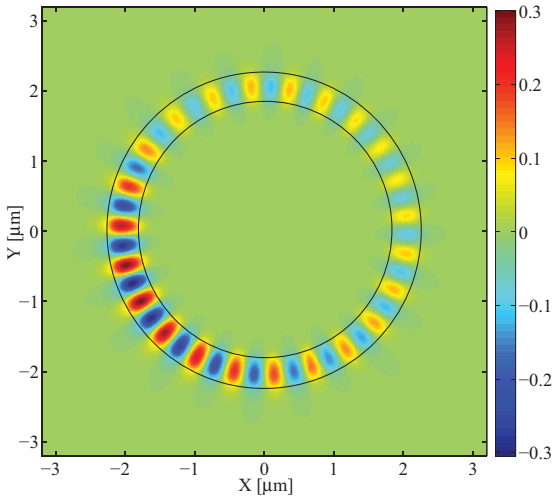

FIG. 5. (Color online) Distribution of E_z at $t = 140$ ps for $M = 23$, using RCN-4 with $\Omega = 4 \times \Omega_0 = 2 \times 10^{11}$ rad/s.

the rotation rate increases to $\Omega = 4 \times \Omega_0$ the Sagnac splitting increases linearly with Ω.

Further, we compare the performance of the two schemes, RCN-2 and RCN-4. Figure 7 shows the spectrum in the band of $M = 23$ for both schemes with two stationary resonances and a couple of split resonances for $\Omega = 10^{12}$ rad/s. The resonances obtained by RCN-2 are slightly lower than those of RCN-4, which is the result of a stronger numerical dispersion experienced by the first scheme. The difference between the splittings of the two schemes is small because the number of points per wavelength inside the resonator is 27.3, which is a relatively high number, but if we look at a much higher mode, the superiority of RCN-4 becomes more obvious.

Figure 8 shows the results of a simulation for the mode $M = 37$, for which the number of points per wavelength inside the medium is 17. Here the numerical dispersion is noticeably more severe for the RCN-2 scheme since it lowers all the resonant frequencies twice as much as previously for $M = 23$. Also, the splitting is reduced by 0.5% from 133.04 GHz for

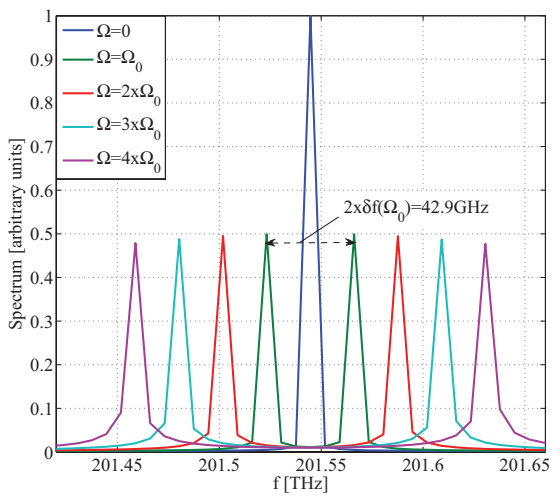

FIG. 6. (Color online) Spectrum vs frequency showing the resonances for stationary resonator and with linearly growing rotation rates for $M = 23$ using RCN-4 scheme.

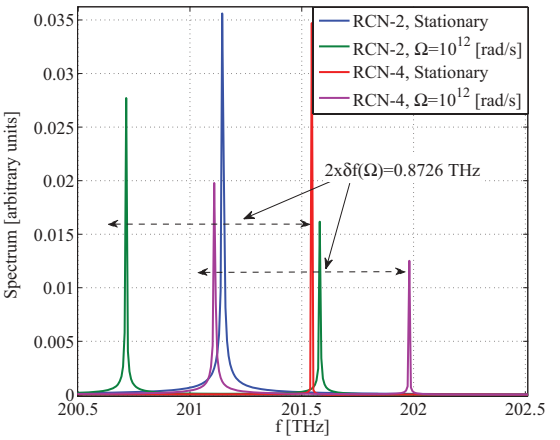

FIG. 7. (Color online) Resonances of both RCN-2 (left) and RCN-4 (right) schemes for $M = 23$ ($n_{\text{eff}} = 2.7225$, $\lambda/n_{\text{eff}}/\Delta x = 27.3$) with $\Omega = 0$ (Stationary) and $\Omega = 10^{12}$ rad/s.

the RCN-4 scheme to 132.32 GHz for RCN-2. Using a coarser grid or looking at higher resonances will result in a much greater difference between the two schemes.

In order to answer the question of which value of the refractive index (group or effective) should be used in Eq. (4.1) we take a look at Fig. 9. It shows the values of the Sagnac splitting obtained by RCN-4 with $\Omega = 10^{12}$ rad/s and those where Eq. (4.1) was used with resonant frequency and the group index was obtained by stationary RCN-4 simulation. We see a very good correspondence between the curve for RCN-4 with rotation (lowest) and the one (which is slightly above) obtained using the group refractive index in the classical expression. The relative difference between the numerical RCN-4 results and the classical Sagnac expression when using the effective index of material is shown in Fig. 10. For higher modes, or alternatively higher frequencies, the difference becomes less substantial. We also checked the results for consistency with the perturbation theory for rotating degenerate microcavities [7]. The theory requires only the knowledge of all the stationary linearly independent modes

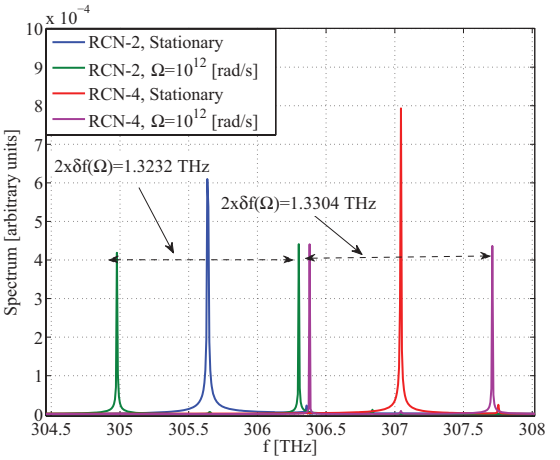

FIG. 8. (Color online) Resonances of both RCN-2 (left) and RCN-4 (right) schemes for $M = 37$ ($n_{\text{eff}} = 2.8748$, $\lambda/n_{\text{eff}}/\Delta x = 17$) with $\Omega = 0$ (Stationary) and $\Omega = 10^{12}$ rad/s.

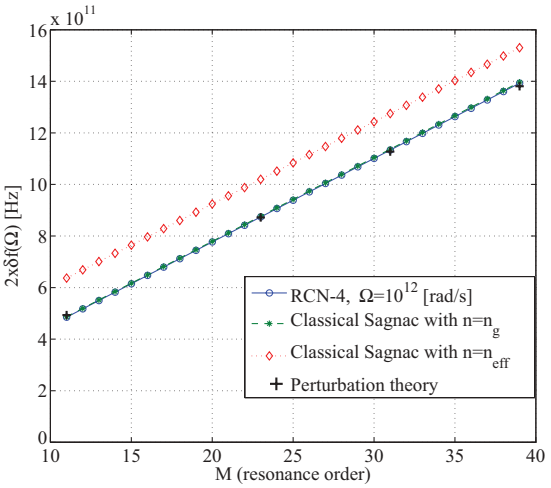

FIG. 9. (Color online) Sagnac resonance splitting vs resonance order.

of the cavity with the same resonant frequency. Since we are dealing with a ring resonator, it has only two linearly independent modes for each resonant frequency (where each mode travels in the opposite direction). Therefore we used a stationary RCN-4 scheme to find the distribution of the magnetic fields $[H_{0x}^{(1,2)}(r)$ and $H_{0y}^{(1,2)}(r)]$ from which we obtained $E_{0z}^{(1,2)}(r)$ using the identity $\vec{\nabla} \times H_0^{(m)} = -i\omega_0\varepsilon_0\varepsilon_r E_0^{(m)}$ where ω_0 is the resonant frequency, ε_r is the relative permittivity of the medium, and m refers to one of the two independent modes. The need to employ this identity comes from the fact that the perturbation theory uses frequency domain, while the fields we get from the RCN-4 are given in time domain; therefore there might be a phase term associated with them. The use of the identity overcomes this problem. In case we deal with an odd numbered resonance M, finding the two independent modes can be done by using excitations at two different places in the resonator. First we run a simulation where the excitation is placed at 12 o'clock in the resonator to obtain $H_{0x}^{(1)}(r)$, $H_{0y}^{(1)}(r)$, and $E_{0z}^{(1)}(r)$. At the second run the excitation is placed at 3 o'clock in the resonator to obtain $H_{0x}^{(2)}(r)$, $H_{0y}^{(2)}(r)$, and $E_{0z}^{(2)}(r)$. This way we get two linearly independent degenerate modes of the resonator shifted by a quarter of a wavelength or $\pi/2$ relative to each other. For example, the distributions of $E_{0z}^{(1)}(r)$ and $E_{0z}^{(2)}(r)$ for $M = 23$ are illustrated in Figs. 11 and 12, respectively.

The same procedure was performed for the modes $M = 11$, $M = 31$, and $M = 39$. The Sagnac frequency splitting values for these resonant modes found using the perturbation theory are marked in Fig. 9. A good agreement with the splitting predicted by the RCN-4 scheme is evident (the error is less than 1%). Hence, we conclude that the Sagnac effect is modeled correctly by the proposed discretization of the Maxwell's equations. We should mention that using only two points in the grid to calculate the fields in the "missing" points, unlike Eq. (2.7) which uses six points, would result in lower values for the Sagnac splitting than predicted by the theory.

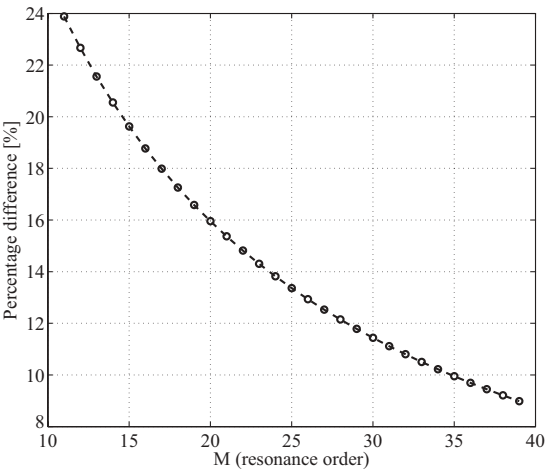

FIG. 10. Relative frequency splitting difference in percent between the classical Sagnac with $n = n_{\text{eff}}$ and RCN-4 scheme for $\Omega = 10^{12}$ rad/s.

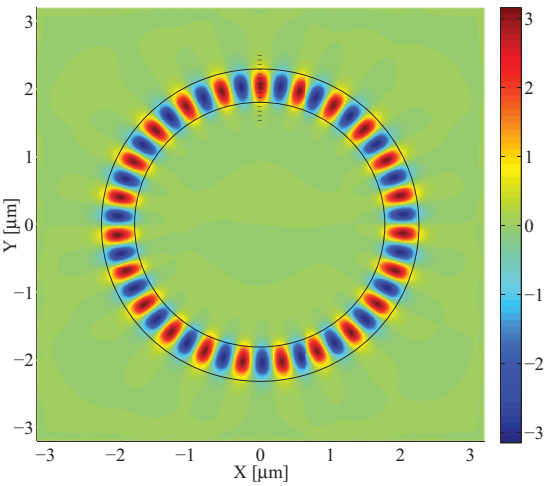

FIG. 11. (Color online) Distribution of the electric field $E_{0z}^{(1)}$ for $M = 23$ calculated using RCN-4 scheme with $\Omega = 0$. The excitation was placed at 12 o'clock in the resonator as indicated.

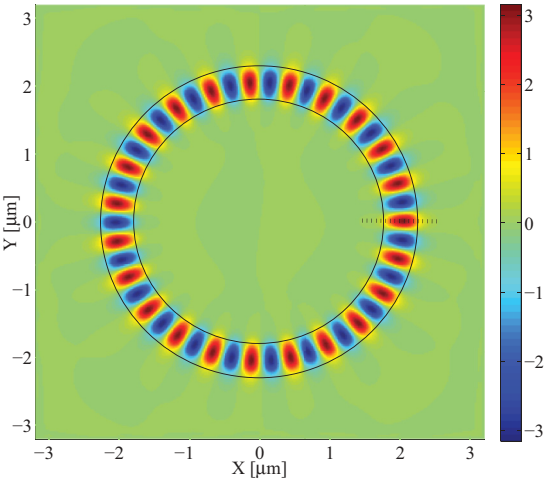

FIG. 12. (Color online) Distribution of the electric field $E_{0z}^{(2)}$ for $M = 23$ calculated using RCN-4 scheme with $\Omega = 0$. The excitation was placed at 3 o'clock in the resonator as indicated.

The dependence of the Sagnac frequency splitting on the group indices of a dispersive medium was previously predicted in Ref. [19]. This result also holds for a medium with only structural dispersion, such as the ring resonator simulated here. This dependence can be shown as follows. The two counterpropagating waves inside the rotating resonator accumulate the phases as

$$\frac{\omega_0}{c} n_{\text{eff}}(\omega_0) L + \Delta\phi = \frac{\omega_0 + \delta\omega(\Omega)}{c} n_{\text{eff}}[\omega_0 + \delta\omega(\Omega)] L, \tag{4.2a}$$

$$\frac{\omega_0}{c} n_{\text{eff}}(\omega_0) L - \Delta\phi = \frac{\omega_0 - \delta\omega(\Omega)}{c} n_{\text{eff}}[\omega_0 - \delta\omega(\Omega)] L, \tag{4.2b}$$

where $L = 2\pi R$ is the resonator's circumference, $n_{\text{eff}}(\omega_0)$ is the effective index of the stationary mode with a resonant frequency ω_0, and $\delta\omega(\Omega)$ and $\Delta\varphi$ are the Sagnac frequency splitting and phase shift respectively, where the latter is given by $\Delta\varphi = \omega_0 L \Omega R / c^2$ [18]. Subtracting Eq. (4.2a) from Eq. (4.2b) and expanding the effective indices at the new resonant frequencies using a Taylor's series up to the first order as

$$n_{\text{eff}}[\omega_0 \pm \delta\omega(\Omega)] \cong n_{\text{eff}}(\omega_0) \pm \delta\omega(\Omega) \left.\frac{dn_{\text{eff}}}{d\omega}\right|_{\omega=\omega_0}, \tag{4.3}$$

we get the following expression for the Sagnac frequency splitting:

$$\delta\omega(\Omega) = \frac{c}{L} \frac{\Delta\phi}{n_{\text{eff}}(\omega_0) + \omega_0 \left.\frac{dn_{\text{eff}}}{d\omega}\right|_{\omega=\omega_0}} = \omega_0 \frac{\Omega R}{c n_g}. \tag{4.4}$$

This expression is identical to that in Eq. (4.1) with the refractive index replaced by the group refractive index. Therefore, in a rotating ring resonator with high dispersion we must employ Eq. (4.4) in order to model the Sagnac effect more accurately.

B. CROW

In this section we apply the RCN-4 to a CROW consisting of four resonators in the form of a racetrack. The distances between the input (output) waveguides and the first (last) resonator is 120 nm, while the distance between two adjacent resonators is 360 nm. All four ring resonators are made of material with the refractive index $n = 3$ and having a radius

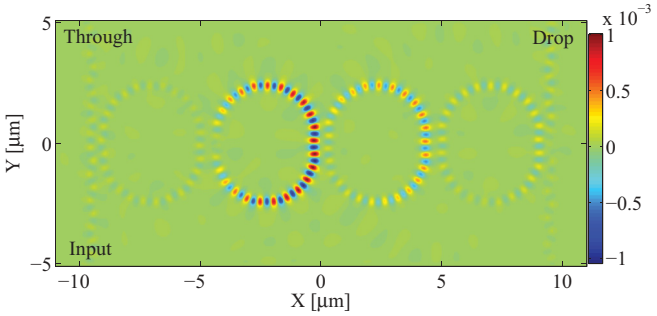

FIG. 13. (Color online) Distribution of E_z at $t = 35$ ps, using RCN-4 with $\Omega = 1.5 \times \Omega_0$.

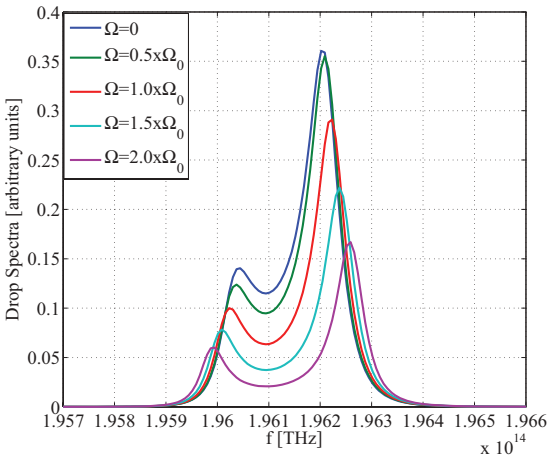

FIG. 14. (Color online) Drop spectra of a CROW for $M = 24$.

of $R = 2$ μm, width of $w = 0.4$ μm, and the straight section length is 0.8 μm. We launched a modulated Gaussian pulse at the input while sampling the electric field at the Through and Drop ports. The center frequency of the pulse corresponds to the radial mode of $M = 25$ of a single resonator, but the pulse was wide enough to also contain the adjacent modes $M = 24$, 26. The simulation was performed for a stationary CROW and for four rotation rates, which were multiples of $\Omega_0 = 10^{11}$ rad/s. The simulations ran up to $t = 35$ ps, where afterwards the field samples were negligibly small, so that we could use zero-padding to acquire the desirable spectrum resolution at the postprocessing phase. The distribution of the E_z field at the end of the simulation is shown in Fig. 13 for $\Omega = 1.5 \times \Omega_0$.

Using the Fourier transform we obtained the spectrum of the Drop port, which is shown, for $M = 24$, in Fig. 14. As the rotation rate increases, a rotation-induced gap (RIG) is formed at the transmission frequencies of the Drop port [20]. Note that the distances between the input (output) waveguide and the first (last) resonator are not identical to the inter-resonator distances; hence the local resonances are not identical along the CROW. These facts, together with a (low-level) loss, create nonsymmetric response curves. This is similar to the structural disorder of a fabricated CROW having slightly different resonators. The evident decrease of the drop signal intensity as a function of rotation rate is a direct consequence of the RIG effect, and has not been observed before in full wave simulations.

V. CONCLUSIONS

In this paper we presented two FDTD schemes for modeling the Sagnac effect in rotating optical elements. The RCN-4 scheme is fourth order accurate in space, and as a result, it shows better accuracy than its second order counterpart RCN-2. The RCN-4 scheme is shown to have lower numerical dispersion with a much better directional isotropy. Both schemes are unconditionally stable and nondissipative. Application of the RCN-4 to a rotating ring resonator showed good correspondence with the theory. We showed that the

Sagnac frequency splitting depends on the group refractive indices of the resonant modes and not solely on the effective indices as in the classical Sagnac expression. The results were also verified against those obtained using the perturbation theory where only the stationary resonant modes are required, showing good agreement with each other. Application of the RCN-4 to a rotating CROW showed a formation of a rotation-induced gap at the center of its transfer function as predicted by the asymptotic methods.

ACKNOWLEDGMENT

This research was supported by the Israel Science Foundation (Grant No. 1423/08).

APPENDIX

In this section we study the instability problem associated with the approach proposed in Ref. [9]. Following similar steps, and neglecting the c^{-4} terms, the Maxwell's equations for the TM mode can be written as

$$\frac{\partial H_x}{\partial t} = -\frac{1}{\mu}\frac{\partial E_z}{\partial y} - \frac{c^{-2}\Omega x}{\mu\varepsilon}\left(\frac{\partial H_y}{\partial x} - \frac{\partial H_x}{\partial y}\right), \tag{A1}$$

$$\frac{\partial H_y}{\partial t} = \frac{1}{\mu}\frac{\partial E_z}{\partial x} - \frac{c^{-2}\Omega y}{\mu\varepsilon}\left(\frac{\partial H_y}{\partial x} - \frac{\partial H_x}{\partial y}\right), \tag{A2}$$

$$\frac{\partial E_z}{\partial t} = \frac{1}{\varepsilon}\left(\frac{\partial H_y}{\partial x} - \frac{\partial H_x}{\partial y}\right) - \frac{c^{-2}\Omega y}{\mu\varepsilon}\frac{\partial E_z}{\partial x} + \frac{c^{-2}\Omega x}{\mu\varepsilon}\frac{\partial E_z}{\partial y}. \tag{A3}$$

Using Yee's lattice together with the leapfrog time discretization the latter equations are

$$\frac{H^{n+1/2}_{x(i,j+1/2)} - H^{n-1/2}_{x(i,j+1/2)}}{\Delta t} = -\frac{1}{\mu_{(i,j+1/2)}}\frac{E^n_{z(i,j+1)} - E^n_{z(i,j)}}{\Delta y} - \left(\frac{c^{-2}\Omega x}{\mu\varepsilon}\right)_{(i,j+1/2)}\left(\frac{\partial H_y}{\partial x} - \frac{\partial H_x}{\partial y}\right)\Bigg|^n_{(i,j+1/2)}, \tag{A4}$$

$$\frac{H^{n+1/2}_{y(i+1/2,j)} - H^{n-1/2}_{y(i+1/2,j)}}{\Delta t} = \frac{1}{\mu_{(i+1/2,j)}}\frac{E^n_{z(i+1,j)} - E^n_{z(i,j)}}{\Delta x} - \left(\frac{c^{-2}\Omega y}{\mu\varepsilon}\right)_{(i+1/2,j)}\left(\frac{\partial H_y}{\partial x} - \frac{\partial H_x}{\partial y}\right)\Bigg|^n_{(i+1/2,j)}, \tag{A5}$$

$$\begin{aligned}\frac{E^{n+1}_{z(i,j)} - E^n_{z(i,j)}}{\Delta t} = {} & \frac{1}{\varepsilon_{(i,j)}}\left(\frac{H^{n+1/2}_{y(i+1/2,j)} - H^{n+1/2}_{y(i-1/2,j)}}{\Delta x} - \frac{H^{n+1/2}_{x(i,j+1/2)} - H^{n+1/2}_{x(i,j-1/2)}}{\Delta y}\right) \\ & - \left(\frac{c^{-2}\Omega y}{\mu\varepsilon}\right)_{(i,j)}\frac{\partial E_z}{\partial x}\Bigg|^{n+1/2}_{(i,j)} + \left(\frac{c^{-2}\Omega x}{\mu\varepsilon}\right)_{(i,j)}\frac{\partial E_z}{\partial y}\Bigg|^{n+1/2}_{(i,j)}.\end{aligned} \tag{A6}$$

The spatial derivatives associated with rotation require the values of the fields at the time midsteps which are missing, that is, H^n_x and H^n_y when calculating them at $n+\frac{1}{2}$, and $E^{n+(1/2)}_z$ when calculating E^{n+1}_z. If we use the linear extrapolation in time as suggested in Ref. [9] to evaluate the missing values based on the two previously calculated values, we get the following set of equations after applying the Fourier transform method [14]:

$$\begin{aligned}\tilde{H}_x \sin\left(\frac{\omega\Delta t}{2}\right) = {} & \frac{1}{\mu}\frac{\Delta t}{\Delta y}\sin\left(\frac{\beta_y\Delta y}{2}\right)\tilde{E}_z \\ & - \Omega m\Delta x\left(\frac{3}{2}e^{-j\omega\frac{\Delta t}{2}} - \frac{1}{2}e^{-j\omega\frac{3\Delta t}{2}}\right)\left[\frac{\Delta t}{2\Delta y}\sin(\beta_y\Delta y)\tilde{H}_x - \frac{\Delta t}{\Delta x}\cos\left(\frac{\beta_y\Delta y}{2}\right)\sin\left(\frac{\beta_x\Delta x}{2}\right)\tilde{H}_y\right],\end{aligned} \tag{A7}$$

$$\begin{aligned}\tilde{H}_y \sin\left(\frac{\omega\Delta t}{2}\right) = {} & \frac{1}{\mu}\frac{\Delta t}{\Delta x}\sin\left(\frac{\beta_x\Delta x}{2}\right)\tilde{E}_z \\ & - \Omega n\Delta y\left(\frac{3}{2}e^{-j\omega\frac{\Delta t}{2}} - \frac{1}{2}e^{-j\omega\frac{3\Delta t}{2}}\right)\left[\frac{\Delta t}{\Delta y}\cos\left(\frac{\beta_x\Delta x}{2}\right)\sin\left(\frac{\beta_y\Delta y}{2}\right)\tilde{H}_x - \frac{\Delta t}{2\Delta x}\sin(\beta_x\Delta x)\,\tilde{H}_y\right],\end{aligned} \tag{A8}$$

$$\begin{aligned}\tilde{E}_z \sin\left(\frac{\omega\Delta t}{2}\right) = {} & \frac{1}{\varepsilon}\frac{\Delta t}{\Delta y}\sin\left(\frac{\beta_y\Delta y}{2}\right)\tilde{H}_x - \frac{1}{\varepsilon}\frac{\Delta t}{\Delta x}\sin\left(\frac{\beta_x\Delta x}{2}\right)\tilde{H}_y \\ & + \Omega\left(\frac{3}{2}e^{-j\omega\frac{\Delta t}{2}} - \frac{1}{2}e^{-j\omega\frac{3\Delta t}{2}}\right)\left[\frac{m\Delta y\Delta t}{2\Delta x}\sin(\beta_x\Delta x) - \frac{n\Delta x\Delta t}{2\Delta y}\sin(\beta_y\Delta y)\right]\tilde{E}_z.\end{aligned} \tag{A9}$$

The term $(\frac{3}{2}e^{-j\omega(\Delta t/2)} - \frac{1}{2}e^{-j\omega(3\Delta t/2)})$ in the equations is complex and is the consequence of the linear extrapolation based on values of the fields in the previous time steps. Since all other terms in the equations are real (including the amplitudes $\tilde{H}_x$, $\tilde{H}_y$, and $\tilde{E}_z$), the three equations can only be satisfied by a complex ω which will give rise to exponentially growing fields. Therefore such a scheme is unstable for any Δt. Another way to look at it is to say that the "effective" rotation rate is $\Omega(\frac{3}{2}e^{-j\omega(\Delta t/2)} - \frac{1}{2}e^{-j\omega(3\Delta t/2)})$ which, in case of a ring resonator, will result in two complex resonance frequency shifts. One mode will have a positive imaginary part in the resonance frequency and it therefore will decay, while the other mode will have a negative imaginary part in the resonance frequency resulting in exponential growth and instability.

[1] G. Sagnac, C. R. Acad. Sci. **95**, 708 (1913).
[2] S. Sunada and T. Harayama, Phys. Rev. A **74**, 021801 (2006).
[3] C. Peng, Z. Li, and A. Xu, Opt. Express **15**, 3864 (2007).
[4] B. Z. Steinberg, Phys. Rev. E **71**, 056621 (2005).
[5] D. Hah and D. Zhang, Opt. Express **18**, 18200 (2010).
[6] J. Scheuer and A. Yariv, Phys. Rev. Lett. **96**, 053901 (2006).
[7] B. Z. Steinberg and A. Boag, J. Opt. Soc. Am. B **24**, 142 (2007).
[8] B. Z. Steinberg, A. Shamir, and A. Boag, Phys. Rev. E **74**, 016608 (2006).
[9] C. Peng, R. Hui, X. Luo, Z. Li, and A. Xu, Opt. Express **16**, 5227 (2008).
[10] R. Sarma, H. Noh, and H. Cao, J. Opt. Soc. Am. B **29**, 1648 (2012).
[11] C. Sun and C. W. Trueman, Electron. Lett. **39**, 595 (2003).
[12] T. Shiozawa, Proc. IEEE **61**, 1694 (1973).
[13] J. L. Anderson and J. W. Ryon, Phys. Rev. **181**, 1765 (1969).
[14] J. W. Thomas, *Numerical Partial Differential Equations* (Springer-Verlag, New York, 1998).
[15] G. W. Stewart, *Matrix Algorithms* (Society for Industrial and Applied Mathematics, Philadelphia, PA, 2001).
[16] B. Finkelstein and R. Kastner, J. Comput. Phys. **221**, 422 (2007).
[17] J. P. Berenger, J. Comput. Phys. **114**, 185 (1994).
[18] E. J. Post, Rev. Mod. Phys. **39**, 475 (1967).
[19] M. S. Shahriar, G. S. Pati, R. Tripathi, V. Gopal, M. Messall, and K. Salit, Phys. Rev. A **75**, 053807 (2007).
[20] B. Z. Steinberg, J. Scheuer, and A. Boag, J. Opt. Soc. Am. B **24**, 1216 (2007).